RSC Advances

ROYAL SOCIETY OF CHEMISTRY

www.rsc.org/advances

RSC Advances

ARTICLE

Kondo-like electronic transport and ferromagnetic cluster-glass behavior in $La_{0.7}Sr_{0.3}MnO_3$ nanostructures

Received 00th January 20xx,
Accepted 00th January 20xx

DOI: 10.1039/x0xx00000x

www.rsc.org/

Hilal Ahmad Reshi[a], Shreeja Pillai[a], Rama Shanker Yadav[a], Touseef Ahmad Para[a], U. P. Deshpande[b], T. Shripathi[b], Vilas Shelke[a*]

We have studied electronic transport and magnetic properties of nanocrystalline $La_{0.7}Sr_{0.3}MnO_3$ system. The samples were prepared by sol-gel method and were sintered at different temperatures to achieve few nanometre grain sizes. The temperature dependent resistivity revealed Kondo like electronic transport at low temperature (T <50 K) and variable range hopping in the paramagnetic insulating regime under zero and high magnetic field. The reduced grain size sample showed marginal increase in electrical resistivity. The temperature-field dependent ac-susceptibility measurement indicated the FM-cluster formation. A neck like magnetic hysteresis loop was observed due to the competition between ferromagnetic core and paramagnetic shell. The ferromagnetic clusters with paramagnetic interfaces impart glassy behavior.

A. Introduction

The discovery of colossal magnetoresistance in rare earth manganites generated intensive stir from fundamental as well as application point of view[1-3]. A widely studied aspect of doped manganite systems has been paramagnetic to ferromagnetic and insulator to metal transitions as a function of divalent substitution. Among the doped perovskite manganites, $La_{1-x}Sr_xMnO_3$ ($0.17 \leq x \leq 0.33$) system has received a lot of attention because of high Curie temperature (T_c), excellent metallic/magnetic behavior, nearly 100 % spin polarization etc. It became a model system for potential applications in terms of Spintronics, sensors, memories, and fuel cell types of devices[4-8]. This system coupled with recent advances in nanomaterials synthesis created new cognizance for materials science research. The most intriguing topics regarding the electrical and magnetic behavior of this system are finite size or low dimensionality effects.

Nanoscale has been a subject of intense research in the past few years due the potential applications at reduced size and dimensionality[9]. Some interesting properties associated with the finite size effect were revealed in perovskite manganites through influence of structural and magnetic disorders at the grain boundaries[10-14]. The size effects and more surface area of nanoparticles can remarkably change certain properties as compared to bulk counterparts. Some of the interesting features displayed by magnetic nanomaterials are low magnetization, high resistivity and low field magnetoresistance[13-15]. The manganites continue to surprise through splendour of electrical transport and magnetic properties. The strong correlations between charge, lattice, orbital and spin degrees of freedom keep changing with thermodynamic variables like composition, temperature, magnetic field and also the grain size. The multiple interactions are difficult to understand in these correlated electron systems. Kondo effect is one such paradigm of electron-correlated physics[16]. The Kondo phenomenon caught interest and recognition in the context of diluted magnetic and quantum dot systems[17-19]. Recently, tunable Kondo effect has been reported in disordered graphene[20, 21]. The characteristic change in electrical resistivity with temperature depends on several intrinsic and extrinsic factors. Instead of saturating, the electrical resistivity increases as the temperature is lowered further.

The grain size effect on electrical, magnetic and magneto-transport properties of manganites has been widely reported[22-24]. These reports mostly focused on near room temperature or transition temperature regime. Small particle size and low temperature can reveal distinct features. In this paper, we report a detailed study regarding the nanosize effect on low temperature electrical and magnetic properties of $La_{0.7}Sr_{0.3}MnO_3$ (LSMO) samples. In bulk form, the composition $La_{0.7}Sr_{0.3}MnO_3$ shows metallic behavior without metal-insulator transition. However, we observed metal-insulator transition followed by sharp upturn in low temperature regime of resistivity-temperature curves in LSMO nanomaterial samples. The low temperature resistivity data fitted well with the equation containing Kondo effect term. The magnetic behavior observed through vibrating sample magnetometer and ac-susceptibility techniques indicated formation of clusters with ferromagnetic cores and paramagnetic shells. It means that the Kondo effect can occur in core-shell structured magnetic system also.

[a] Novel Materials Research Laboratory, Department of Physics, Barkatullah University, Bhopal 462026 INDIA * e mail- drshelke@gmail.com
[b] UGC-DAE Consortium for Scientific Research, DAV Campus, Khandwa Road, Indore 452017 INDIA

B. Experimental Techniques

Nanostructured samples with nominal composition $La_{0.7}Sr_{0.3}MnO_3$ were prepared by a solution derived sol-gel technique[25]. The stoichiometric amounts of $(CH_3COO)_2La.xH_2O$, $(CH_3COO)_2Mn.4H_2O$ and $(CH_3COO)_2Sr.aq$ were used as starting materials. The precursors of final solution were prepared by dissolving the chemicals in 100 ml distilled water with 30 ml of acetic acid. The precursors were stirred and heated continuously at 160 °C to make a homogeneous solution. 100 ml ethylene glycol was poured into the solution, when most of the distilled water was evaporated. The pH was maintained around neutral value by adding ammonium acetate solution. The solution was continuously stirred and heated to eliminate the excess reagents and water to form dark brown gel. The final form of gel was grinded for an hour and was calcined at 500 °C for 12 hours to obtain black powder. The calcined powder was pressed into pellets, which were sintered at 550 °C (S55) and 600 °C (S60) for 12 hours.

The phase formation and crystal structure of the samples were determined by X-ray diffraction (XRD) method using Cuk_α radiation. The Rietveld analysis of XRD data was performed using FULLPROF computer tool. The chemical compositions were determined by X-ray Photoelectron spectroscopy (Specs, Germany) with AlKα source (excitation energy 1486.6 eV). The average particle size of the samples was determined using transmission electron microscopy (TEM). Conventional four probe technique was used in the temperature range 5 K ≤ T ≤ 300 K at 0 and 8 tesla magnetic field for the transport and magnetotransport properties measurement. The temperature versus ac magnetic susceptibility was measured at 131Hz frequency and 2.5 to 10 Oe magnetic fields. The field dependence of magnetization was measured at 10 K temperature using vibrating sample magnetometer (VSM).

C. Results and Discussion

Structural Analysis

The X-Ray Diffraction patterns of the $La_{0.7}Sr_{0.3}MnO_3$ samples sintered at 550^0 C (S55) and 600^0 C (S60) are shown in fig. 1 a) and b) respectively. The data was fitted with Rietveld refinement to obtain the structural parameters. The samples revealed pure LSMO phase with no detectable secondary phase. The crystal structure belonged to orthorhombic *Pnma* space group. The X-ray profiles were modelled using a pseudo-voigt shape function. The refined structural parameters for S55 and S60 samples obtained through Rietveld analysis are listed in Table 1. Most of the polycrystalline and single crystal samples show rhombohedral structure. Nonetheless, there are few reports on the orthorhombic structure for this composition[25,26]. The corresponding reliability factor χ^2 (R_{wp}/R_{exp}), also sometimes called as goodness of fit has values 2.29 and 1.54 for samples S55 and S60 respectively. A better fit can be obtained for bulk materials data. In case of nanomaterials, peak shape broadening and structural modulations due to crystal strain impart slight deviation. The sample S55 sintered at lower temperature has lower unit cell volume than sample S60. The lower unit cell volume may be the consequence of cationic/anionic vacancies. The rate of oxygen in-diffusion is less at lower sintering temperature.

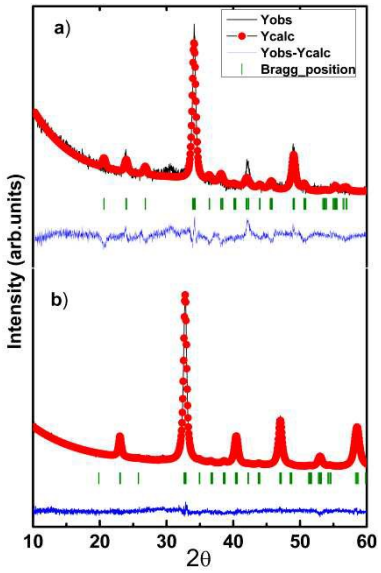

Fig. 1 The Rietveld fitted XRD patterns of LSMO samples a) S55 and b) S60

Table 1 Rietveld refined structural parameters of S55 and S60 samples for orthorhombic (pnma) space group

Parameters	Sample S55	Sample S60
a (Å)	5.342	5.446
b (Å)	7.444	7.712
c (Å)	5.261	5.487
V (Å^3)	209.24	230.51
La^{+3}		
x	0.0869	0.0148
y	0.2500	0.2500
z	0.9982	0.0114
Mn^{+3}		
x	0.0000	0.0000
y	0.0000	0.0000
z	0.5000	0.5000
O_1^{-2}		
x	-0.1293	0.5041
y	0.2500	0.2500
z	-0.0372	-0.0090
O_2^{-2}		
x	0.6374	0.2009
y	0.0065	0.0221
z	1.2063	0.6819
χ^2	2.29	1.54

Chemical composition

The XPS spectra for various constituent elements of the samples S55 and S60 are shown in Fig 2. The chemical compositions were determined using atomic sensitivity factor and peak area fitted by XPS peak 4.1 software with FWHM consideration for overlapping peaks. The binding energies were rectified after correction of charging effects using C1s peak at 284.5eV. The chemical composition for La:Sr:Mn:O elements was found around 14.7:7.7:16.1:61.5 within accuracy limit of XPS for both the samples. Since none of the constituent was volatile or less reactive, a large deviation from nominal stoichiometry was not expected.

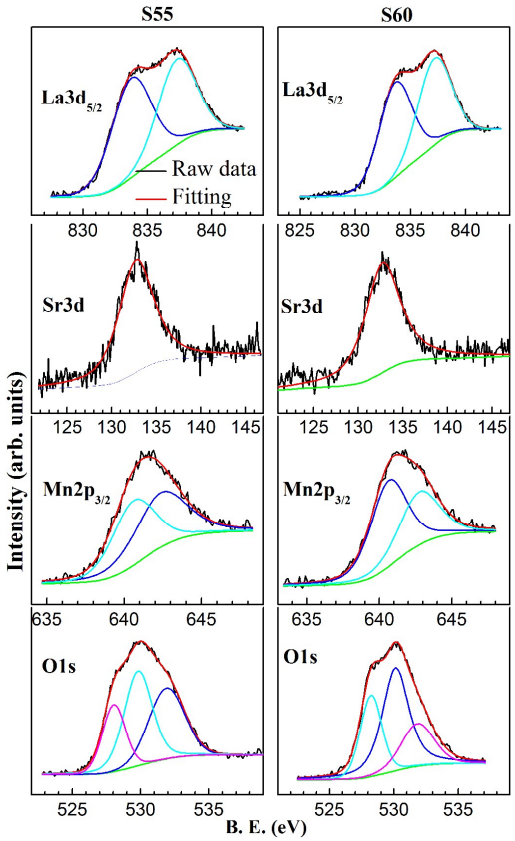

Fig. 2 Core level XPS spectra for various elements in samples S55 and S60

Morphology

The transmission electron microscopy (TEM) images of S55 and S60 samples are shown in fig. 3 a)-b) and d)-e) respectively. The micrographs reveal that the particle size distribution is uniform and the average particle size for S55 and S60 samples are 16 and 22 nm respectively. The high resolution TEM images given in fig. 3 b) and e) revealed single-phase lattice resolved planes and grain interfaces. The selected area electron diffraction (SAED) patterns in Fig 3 c) and f) indicate the polycrystalline nature of the samples[27]. The crystalline nature improved with increasing sintering temperature.

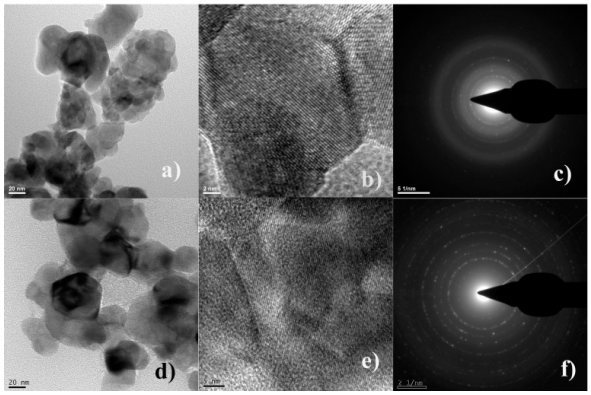

Fig. 3 Transmission Electron Microscopy (TEM) images with SAED patterns of a)-c) S55 and d)-f) S60 nanostructured LSMO samples.

Electrical behavior

The variation of electrical resistivity as a function of temperature with a zero and high magnetic field (8 tesla) is shown in fig 4 a) and b). The resistivity becomes higher with reducing grain size probably due to the potential barrier at interface layers between grains[28-30]. In bulk LSMO, the metal-insulator transition has not been observed[31, 32], however, in nanostructured LSMO samples such behavior has been reported[33,34]. The metal-insulator transition temperature (T_{MI}) shifts towards lower temperature with decreasing grain size. Below T_{MI} both the samples show gradual resistivity drop up to 50 K followed by rapid upturn at low temperature. The overall resistivity was suppressed significantly on application of high magnetic field. The resistivity minimum shifts towards lower temperature on application of magnetic field. This indicates that low temperature resistivity is sensitive to applied field. This behavior can be attributed to the interference of e-e scattering. However, based on the sensitivity of the resistivity to applied magnetic field, the spin dependent scattering cannot be ruled out[35]. Another counter argument is that additional scattering from spin disordered grain boundaries is responsible for low temperature resistivity behavior[36].

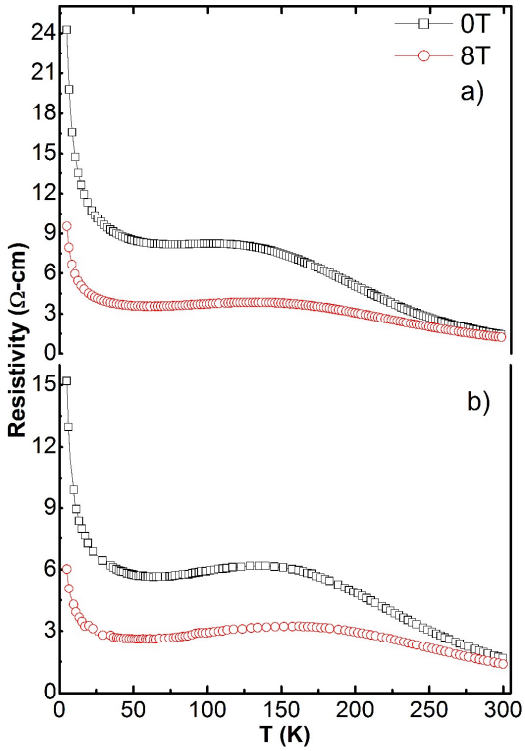

Fig. 4 Temperature dependent electrical resistivity of a) S55 and b) S60 LSMO samples under 0 and 8T magnetic field

The rare earth manganites form a strongly correlated electronic system in which various types of interactions exist in tandem. In addition to universal residual resistivity, temperature dependent electron-phonon (e-p) and electron-electron (e-e) interactions contribute to the net resistivity[37-38]. Moreover, weak localization, inter-granular tunnelling etc also create complex interplay. Nevertheless, all these terms cannot account for the rapid upturn in resistivity below 50 K. In diluted magnetic semiconductors, impure metals and quantum dots such behavior has been attributed to the

existence of Kondo-effect[16-19]. We could fit the low temperature (T<50K) resistivity data to the equation,

$$\rho_L = \rho_o - \rho_s \ln T + \rho_e T^{1/2} + \rho_p T^5 \qquad (1)$$

Where ρ_o is residual resistivity which depends on defects, grain boundary effects and magnetic domain boundary effects; ρ_s is Kondo-like spin-dependent scattering, ρ_e is electron-electron correlation interaction and ρ_p is electron-phonon interaction.

The equation fitted low temperature resistivity curves are shown in figure 5 a) and b). The experimental data fits well with equation (1) and the fitting parameters are given in table 2. The electron-phonon interaction (ρ_p) is several orders smaller in low temperature regime and is not sensitive to the applied field. The e-e interaction (ρ_e) has low contribution and field dependence at in this temperature range. Just below 50K, the resistivity curves are flat approaching towards residual resistivity due to static defects and then they make sharp upturn at lower temperature. The sharp resistivity upturns originate from the dynamical character of localized spin system[16]. In addition to static defects, magnetic domain boundaries, and e-e interaction, the coupling between localized electron spin and sea of conduction electrons hinders the electron motion. The amplitude of exchange interaction between conduction and localized electrons diverges as temperature approaches zero. As a result, the resistivity value increases sharply in low temperature regime. The application of high magnetic field reduces the spin-disorder scattering. Therefore, the resistivity divergence is suppressed significantly. In principle, Kondo effect may be nullified at sufficiently high magnetic field. Zhang et al[39] has reported Kondo-like transport in low bandwidth $La_{2/3}Ca_{1/3}MnO_3$ system along with spin glass phase. Our study indicates that Kondo effect is more generalized phenomenon and can occur in ferromagnetic cluster system. In fact, tunable or disorder mediated Kondo effect in graphene occurs even though carbon lacks d or f electrons[20,21]. The defects in graphene interact magnetically with conduction electrons and restrict their mobility.

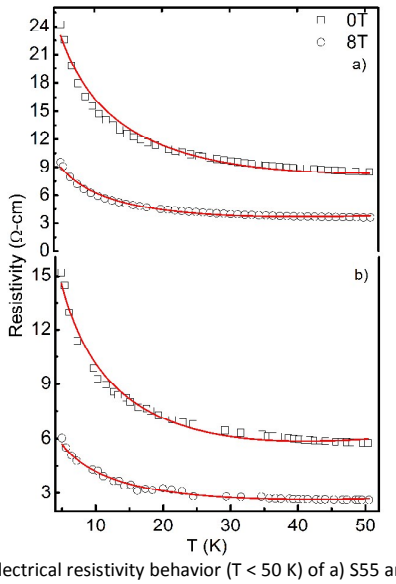

Fig. 5: The electrical resistivity behavior (T < 50 K) of a) S55 and b) S60 LSMO samples. The solid lines correspond to the fit using eq. (1).

Table 2. Fitting parameters obtained from resistivity data using Eq. (1), (2) and (3) for S55 and S60 samples

Parameter	Sample S55		Sample S60	
	H = 0T	H = 8T	H = 0T	H = 8T
ρ_0 (Ω–cm)	38.02	15.08	24.11	9.06
ρ_s (Ω–cm)	15.07	6.63	10.58	3.59
ρ_e (Ω–cmK$^{-1/2}$)	4.13	2.06	3.28	1.07
ρ_p (x10^{-10} Ω–cmK^{-5})	1.3	1.3	1.0	1.2
T_o (x10^6)	11.7	3.96	7.30	2.16
N(E_F) (x10^{26} ev^{-1}cm^{-3})	2.05	5.79	3.14	10.62

The resistivity behavior in high temperature insulating region can be analyzed in terms of lattice polaron formation from strong lattice coupling or Variable Range Hopping (VRH) expression[40]. Our resistivity data in the region above T_{MI} was fitted with VRH expression given by:

$$\rho = \rho_1 \exp (T_0/T)^{1/4} \qquad (2)$$

Where ρ_1 is the residual resistivity and T_0 is the characteristic temperature related to localised states and density of states. The VRH equation fitted curves (lnρ vs. $T^{-1/4}$) are shown in figure 6 a) and b). Both the samples follow VRH model in a satisfactory way with R^2 fitting factor around 0.99. The values of density of states $N(E_F)$ at Fermi level were calculated from T_0 values using equation;

$$T_0 = 18\alpha^3/K_B N(E_F) \qquad (3)$$

Where α is the corresponding localization length with value 0.45 nm for LSMO[41,42]. The calculated parameters given in table 2 are in good agreement with the values reported in literature for other manganites[41,42]. The T_0 values decrease with increasing grain size and magnetic field. Consequently, the values of $N(E_F)$ also increase with increasing grain size.

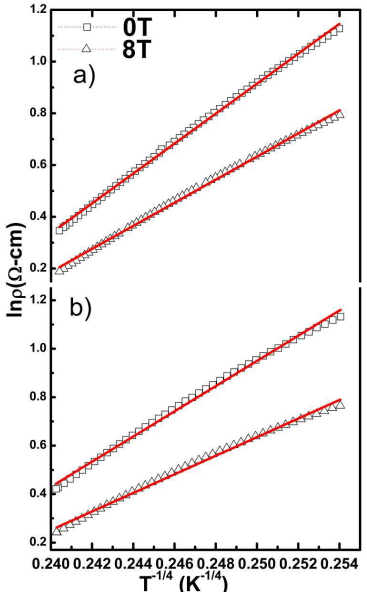

Fig. 6: Variable range hopping (VRH) fit to the resistivity data in the temperature range of 189-300 K for a) S55 and b) S60 samples.

ac Susceptibility Measurement

The variation of real (χ') and imaginary (χ'') ac susceptibility at different fields in the temperature range 75-300 K is shown in figure 7 a) and b) respectively. The susceptibility real (χ') values show gradual increase below room temperature and achieve peak around 210 K. The paramagnetic to ferromagnetic transition temperature (T_c) might be well above 300 K as expected for $La_{0.7}Sr_{0.3}MnO_3$ system[43]. The sample S60 has higher susceptibility values than sample S55 at all temperatures. The susceptibility real values increased slightly for higher applied magnetic field for both samples. The rare-earth manganites are complex systems exhibiting variety of composition, temperature and magnetic field dependent phases. The bulk $La_{0.7}Sr_{0.3}MnO_3$ is ferromagnetic below room temperature. However, the literary consensus disappears for the same composition in nanomaterial form. In addition to formal double exchange interaction, other parameters like size and shape of particles, size distribution, and finite size effect influence the magnetic behavior of nanomaterials. The resulting systems of interacting or non-interacting spins are referred by spin-glass, superparamagnetic, ferromagnetic-cluster glass etc. nomenclatures[44-46]. The primary indication of such distinctness is given by the splitting of FC and ZFC curves of magnetization (M-T) measurements. Further insight can be obtained through frequency or field dependent ac susceptibility measurement. The characteristic peak in χ'-T curve corresponds to the temperature at which thermal activation supersedes magnetic anisotropy energy and is referred as blocking/freezing temperature

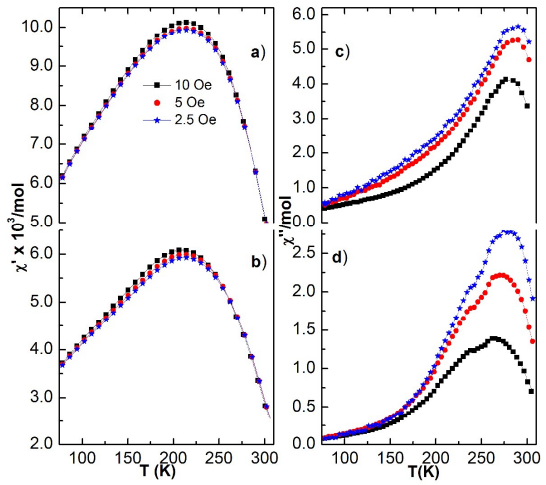

Fig. 7: ac magnetic susceptibility χ' (a and b); χ'' (c and d) of S55 and S60 samples respectively at different magnetic fields.

In our samples, no shifting of peak was observed with change in applied magnetic field. Nevertheless, the imaginary susceptibility values (χ'') did show field dependent variation. The amplitude of χ'' as well as peak temperature shifted towards lower values with increase in magnetic field from 2.5 Oe to 10 Oe. This behavior is contradictory with typical spin-glass system. The ferromagnetic cluster glass interpreted in terms of core-shell model seems more likely possibility[45]. In bulk systems, the grain is homogeneously ferromagnetic as shown schematically in figure 8 a). As the particle size is reduced, the inner core remains the same as bulk sample but outer shell behaves differently due to surface effects like stress, vacancies, broken chemical bonds, etc (figure 8 b). The ferromagnetic coupling or exchange interaction between the shell magnetic moments is weakened considerably. Further decrease in particle size (figure 8 c) creates more disorder in the alignment. If α is the shell/core ratio, the total magnetization will be,

$$M = \alpha M_{shell} \sum_{ij} \cos\theta_{ij} + (1-\alpha) M_{core} \sum_{ij} \cos\theta_{ij} \qquad (4)$$

Where, M_{shell}, M_{core} are the magnetizations for shell and core respectively and θ_{ij} are the angles between spins i, j. The angle may vary from 0° for FM to 180° for AFM orderings. The Heisenberg exchange energy between two neighbouring moments is given by,

$$E_{ex} = -J \sum_{ij} S_i S_j \cos\theta_{ij} \qquad (5)$$

With J as exchange constant, S_i/S_j as spin quantum numbers of spin i, j respectively. The variation of exchange energy with two dimensional radial positions of moments is schematically shown in figure 8 a) - c). An ensemble of such core/shell structures forms ferromagnetic cluster glass which is distinct from spin glass system.

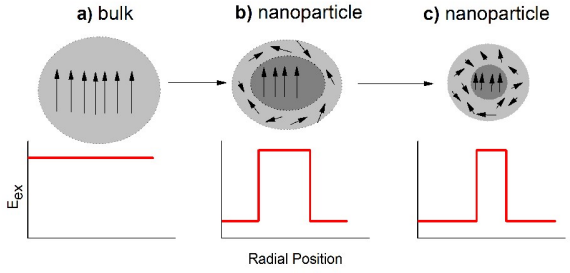

Fig. 8: Schematic diagram of magnetic moments configuration and exchange energy landscape for different particle size on the basis of core-shell model.

Magnetization behavior

A further insight of magnetic behavior was obtained through magnetization measurement as a function of applied magnetic field (H). A representative M-H curve for the sample S60 is shown in figure 9. The hysteresis loop showed signature of ferromagnetic ordering with coercive field of 350 Oe and remnant magnetization 8 emu/gm (upper inset of fig. 9). Indeed, there is distortion in the symmetry of loop and magnetization remained unsaturated up to the magnetic field of 50 KOe. The contribution from FM particle core tends to saturate at low fields and magnetically disordered surface spins remain unsaturated till the highest applied field. The mix behavior can be ascribed to the dissimilar sensitivities of different magnetic phases to the applied field. There is a strong interplay between magnetic disorders at the nanosurfaces, interparticle interactions and FM ordering in the cores of nanograins. The FM cluster moments are polarized under low fields, while the disordered moments keep orienting linearly with increasing magnetic field[47,48]. The neck like hysteresis loop appears due the competition or combination of ordered-disordered magnetic moments. The Arrot plot (M^2 versus H/M) shown in the lower inset

of figure 9 indicates a convex curvature with a finite spontaneous magnetization which is a signature of ferromagnetic phase of the sample. The convex curvature is sharp at low field. At higher magnetic field the plot shows linear rise.

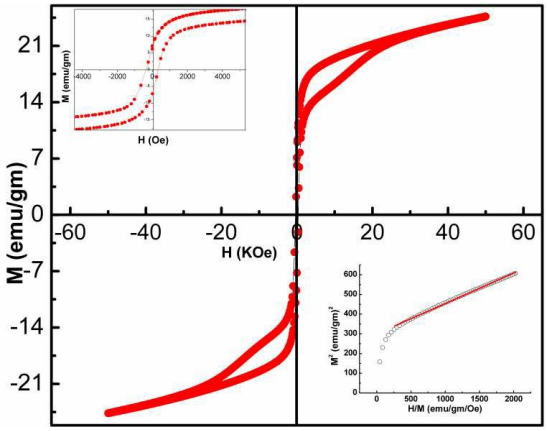

Fig. 9: Magnetization versus applied magnetic field at 10 K of S60 sample. Upper inset- low field region and lower inset- Arrot plot

Conclusion

We have studied electrical transport and magnetic behavior of LSMO samples with few nanometers grain sizes. The samples showed Kondo-like electronic transport features at low temperature (< 50 K) while VRH model fits well within the paramagnetic insulating region without and with applied magnetic field. The ac-susceptibility and field dependent magnetization measurements indicated FM-cluster behavior. The existence of Kondo effect in FM cluster system is the interesting feature for manganite nanomaterial.

Acknowledgement

We are thankful to M. P. Council of Science and Technology, Bhopal and University Grants Commission, New Delhi for providing financial support. Part of this work was performed at UGC-DAE consortium for Scientific Research, Indore. We are especially grateful to Dr. Alok Banerjee, Dr. Rajiv Rawat and Dr. Mukul Gupta, UGC-DAE Consortium for Scientific Research, Indore, India for providing experimental facilities.

Notes and references

1. A-M Haghiri-Gosnet, and J. P. Renard, *J. Phys. D: Appl. Phys*., 2003, **36**, R127.: N. Izyumskaya, Y. Alivov, and H. Morkoc, *Cri. Rev. Solid State Mater. Sci*., 2009, **34**, 89.
2. L. S. Lakshmi, K. Dorr, K. Nenkov, A. Handstein, K. H. Muller, and V. S. Sastry, *J. Phys.: Cond. Matter*, 2007, **19**, 216218.
3. Y. Tian, S. R. Bakaul, and T. Wu, *Nanoscale*, 2012, **4**, 1529.
4. J. Nogues, V. Skumryev, J. Sort, S. Stoyanov, and D. Givord, *Phys. Rev. Lett.*, 2006, **97**, 157203.
5. G. F. Goya, T. S. Berquo, F. C. Fonsecca, and M. P. Morales, *J. Appl. Phys.*, 2003, **94**, 3520.
6. K. Miyazaki, N. Sugimura, K. Matsuoka, Y. Iriyama, T. Abe, M. Matsuoka, and Z. Ogumi, *J. Power Sources*, 2008, **178**, 683.
7. K. Zhang, J. Sunarso, Z. P. Shao, W. Zhou, C. H. Sun, S. B. Wang, and S. M. Liu, *RSC Adv.,* 2011, **1**, 1661.
8. K. L. Yan, R. H. Fan, X. A. Wang, M. Chen, K. Sun, Z. D. Zhang, Q. Hou, L. Qian, S. B. Pan, M. X. Yu, *RSC Adv.,* 2014, **4**, 25804.
9. J. I. Martin, J. Nogues, K. Liu, J. L. Vicent, I. K. Schuller, *J. Magn. Magn. Mater.*, 2003, **256**, 449.
10. V. Markovich, R. Puzniak, I. Fita, D. Mogilyansky, A. Wisniewski, Y. Skourski, G. Jung, and G. Gorodetsky, *J. Nanopart. Res.*, 2013, **15**, 1862.
11. S. Daengsakul, C. Thomas, C. Mongkolachit, S. Maensiri, *Solid State Sci.*, 2012, **14**, 1306.
12. M. Oumezzine, S. Hcini, M. Baazaoui, H. B. Sales, I. M. G. D. Santos, and M. Oumezzine, *J. Alloy. Compd*., 2013, **571**, 79 .
13. H. A. Reshi, S. Pillai, D. Bhuwal, V. Shelke, *J. Nanosci. Nanotechnol.*, 2013, **13**, 4608.
14. T. Sarkar, A. K. Raychaudhuri, A. K. Bera, and S. M. Yusuf, *New J. Phys.,* 2010, **12**, 123026.
15. P. R. Sagdeo, and A. Sagdeo, *Appl. Phys. A*, 2013, **113**, 793.
16. J. Kondo, *Prog. Theoretical Phys.* 1964, **32**, 37; J. R. Schrieffer, *J. Appl. Phys.* 1967, **38**, 1143.
17. W. G. van der Wiel, S. D. Franceschi, T. Fujisawa, J. M. Elzerman, S. Tarucha, L. P. Kouwenhoven, *Science*, 2000, **289**, 2105
18. A. Brinkman, M. Huijben, M. V. Zalk, J. Huijben, U. Zeitler, C. J. Maan, W. G. Van der Wiel, G. Rijnders, D. H. A. Blank, and H. Hilgenkamp, *Nature Mater.*, 2007, **6**, 493.
19. S. Amasha, A. J. Keller, I. G. Rau, A. Carmi, J. A. Katine, H. Shtrikman, Y. Oreg, and D. G. Gordon, *Phys. Rev. Lett.*, 2013, **110**, 046604.
20. J-H. Chen, L. Li, W. G. Cullen, E. D. Williams, and M. S. Fuhrer, *Nature Phys.*, 2011, **07**, 535.
21. V. G. Miranda, L. G. G. V. Dias da Silva, and C. H. Lewenkopf, *Phys. Rev. B*, 2014, **90**, 201101 (R).
22. P. Dutta, P. Dey, and T. K. Nath, *J. Appl. Phys*., 2007, **102**, 073906.
23. P. Dey, and T. K. Nath, *Phys. Rev. B*., 2006, **73**, 214425.
24. A. Dutta, N. Gayathri, and R. Ranganathan, *Phys. Rev. B,* 2003, **68**, 054432.
25. H. A. Reshi, A. P. Singh, S. Pillai, R. S. Yadav, S. K. Dhawan, and V. Shelke, *J. Mater. Chem. C*, 2015, **3**, 820.
26. J. F. Mitchell, D. N. Argyriou, C. D. Potter, D. G. Hinks, J. D. Jorgensen, and S. D. Badar, *Phys. Rev. B*., 1996, **54**, 6172.
27. S. Daengsakul, C. Mongkolkachit, C. Thomas, S. Siri, I. Thomas, V. Amornkitbamrung, and S. Maensiri, *Appl. Phys. A*, 2009, **96**, 691.
28. S. Roy, I. Dubenko, D. D. Edorh, and N. Ali, *J. Appl. Phys.*, 2004, **96**, 1202.
29. M. A. Lopez-Quintela, L. E. Hueso, J. Rivas, and F. Rivadulla, *Nanotechnology,* 2003, **14**, 212.
30. G. D. Dwivedi, M. Kumar, P. Shahi, A. Barman, S. Chatterjee, and A. K. Ghosh, *RSC Adv*., 2015, **5**, 30748.

31. V. Shelke, A. Das, I. Dhiman, R. Yadav, S. Khatarkar, A. Anshul, and R. K. Singh, *J. Phys.: Cond. Mater*, 2008, **20**, 395218.
32. R. Yadav, A. Anshul, and V. Shelke, *J. Mater Sci: Mater Electtron*, 2011, **22**, 1173.
33. K. Das, R. Rawat, B. Satpati, and I. Das, *Appl. Phys. Lett.* 2013, **103**, 202406.
34. P. V. Cuong, J. Dho, H. Y. Park, and D. H. Kim, *Appl. Phys. A*, 2009, **95**, 567.
35. Y. Xu, J. Zhang, G. Cao, C. Jing, and S. Cao, *Phys. Rev. B,* 2006, **73**, 224410.
36. E. Rozenberg, *J. Supercond, Nov. Magn*., 2010, **23**, 183.
37. G. Venkataiah, J. C. A. Huang, and P. V. Reddy, *J. Magn. Magn. Mater*., 2010, **322**, 417.
38. M. Stier, and W. Notling, *Phys. Rev. B,* 2007, **75**, 144409.
39. J. Zhang, Y. Xu, S. Cao, G. Cao, Y. Zhang, and C. Jing, *Phys. Rev. B,* 2005, **72**, 054410.
40. N. F. Mott, Conduction in non-crystalline materials (Oxford: Clarendon Press) 2nd Edn. (1993)
41. M. Viret, L. Ranno, and J. M. D. Coey, *Phys. Rev. B,* 1997, **55**, 8067.
42. S. Datta, S. Chandra, S. Samanta, K. Das, and H. Srikanth, B. Ghosh, *J. Nanomaterials,* 2013, **1**, 162315.
43. N. K. Prasad, L. Hardel, E. Duguet, and D. Bahadur, *J. Magn. Magn. Mater*., 2009, **321**, 1490.
44. V. Markovich, I. Fita, A. Wisniewski, G. Jung, D. Mogilyansky, R. Puzniak, L. Titelman, and G. Gorodetsky, *Phys. Rev. B*, 2010, **81**, 134440.
45. A. Rostamnejadi, H. Salamati, and P. Kameli, *J. Supercond Nov. Magn*., 2012, **25**, 1123.
46. T. Zhang, T. F. Zhou, T. Qian, and X. G. Li, *Phys. Rev.*, 2007, B **76**, 174415.
47. T. Zhang, T. F. Zhou, T. Qian, and X. G. Li, *Phys. Rev. B* **,** 2007, **76**, 174415.
48. T. Zhang, and M. Dressel, *Phys. Rev. B*, 2009, 80, 014435.